Confinement Accelerates Water Oxidation Catalysis: Evidence from In Situ Studies

Kassa Belay Ibrahim,* Tofik Ahmed Shifa, Matteo Bordin, Elisa Moretti, Heng-Liang Wu,* and Alberto Vomiero*

Basic insight into the structural evolution of electrocatalysts under operating conditions is of substantial importance for designing water oxidation catalysts. The first-row transition metal-based catalysts present state-of-the-art oxygen evolution reaction (OER) performance under alkaline conditions. Apparently, confinement has become an exciting strategy to boost the performance of these catalysts. The van der Waals (vdW) gaps of transition metal dichalcogenides are acknowledged to serve as a suitable platform to confine the first-row transition metal catalysts. This study focuses on confining $Ni(OH)_2$ nanoparticle in the vdW gaps of 2D exfoliated SnS_2 (Ex-SnS_2) to accelerate water oxidation and to guarantee long term durability in alkaline solutions. The trends in oxidation states of Ni are probed during OER catalysis. The in situ studies confirm that the confined system produces a favorable environment for accelerated oxygen gas evolution, whereas the un-confined system proceeds with a relatively slower kinetics. The outstanding OER activity and excellent stability, with an overpotential of 300 mV at 100 mA cm^{-2} and Tafel slope as low as 93 mV dec^{-1} results from the confinement effect. This study sheds light on the OER mechanism of confined catalysis and opens up a way to develop efficient and low-cost electrocatalysts.

1. Introduction

Energy crisis and environmental pollution have stimulated researchers to seek sustainable alternatives to non-renewable energy sources. To this end, electrochemical water splitting is a promising strategy for the urgent development of green and affordable energy production.[1,2] It involves the production of H_2 gas at the cathode and O_2 gas at the anode of an electrochemical cell. The oxygen evolution reaction (OER) route suffers from the requirement of an excess overpotential relative to that mandated by the thermodynamic value.[3] This is due to the fact that four concerted proton-coupled electron transformation occurs, which in turn leads to the inherently sluggish kinetics. The development of efficient catalysts to solve this problem would not only make water splitting technologies veritable, but also accelerate kinetics of other sustainable pathways, such as carbon dioxide reduction, rechargeable metal–air batteries, and regenerative fuel cells.[4] In line with this, first-row (3d) transition-metal oxides are promising non-noble electrocatalysts for OER. Different strategies have been used to exploit these materials.[5] Interestingly, they undergo in situ surface reconstruction during OER and turn into another oxide phase. This newly induced phase, apparently, performs better than the parent material. However, these materials (despite their promising performance) tend to aggregate during catalysis, thereby blocking the active sites, which is detrimental to realize efficient catalysis.[6] One credible scheme, to tackle this problem, is employing the concept of confined catalysis[7–12] by using layered 2D materials, whose van der Waals gaps serve as a confining pocket. Recently, 2D transition metal dichalcogenides (TMDs)[13] based confined catalysts have emerged as viable

K. B. Ibrahim, T. A. Shifa, M. Bordin, E. Moretti, A. Vomiero
Department of Molecular Sciences and Nanosystems
Ca' Foscari University of Venice
Mestre 30170, Italy
E-mail: kassabelay.ibrahim@unive.it; alberto.vomiero@ltu.se

K. B. Ibrahim, H.-L. Wu
Center for Condensed Matter Sciences
National Taiwan University
Taipei 10617, Taiwan
E-mail: hengliangwu@ntu.edu.tw

K. B. Ibrahim, H.-L. Wu
Center of Atomic Initiative for New Materials
National Taiwan University
Taipei 10617, Taiwan

A. Vomiero
Division of Materials Science
Department of Engineering Sciences and Mathematics
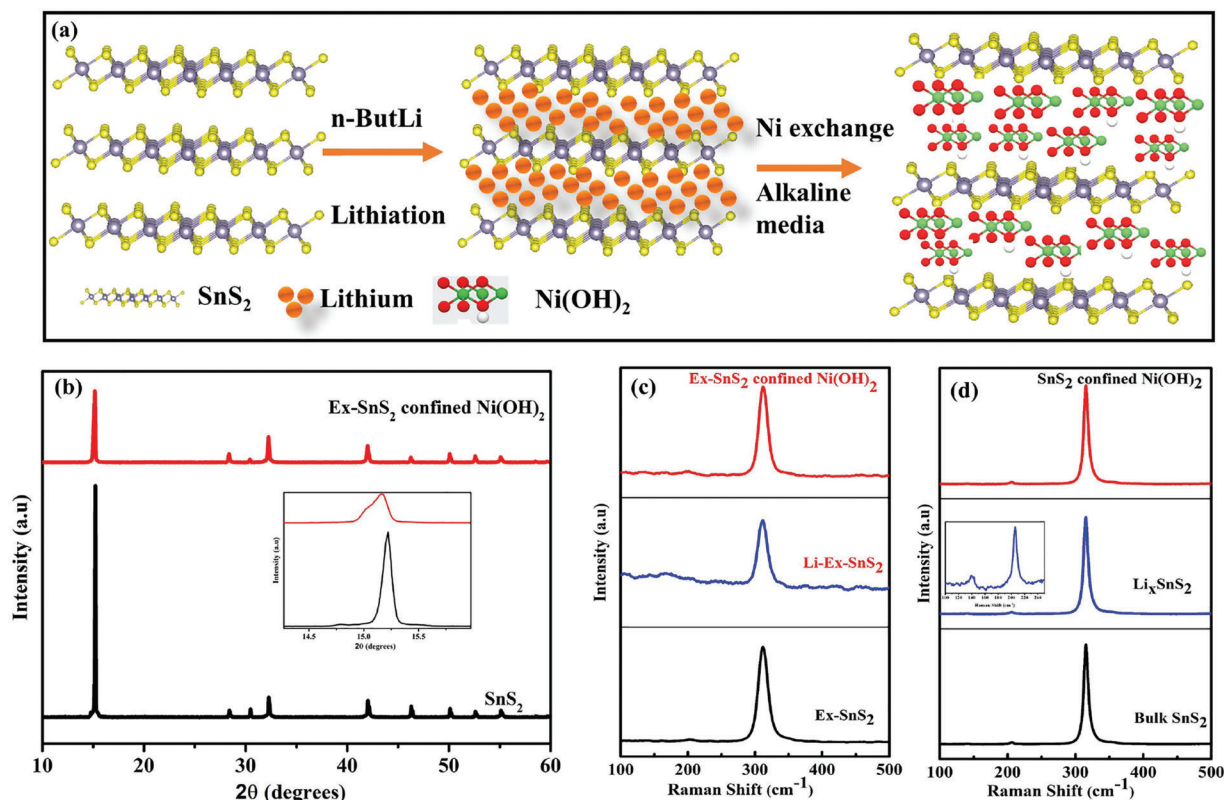Luleå University of Technology
Luleå SE-97187, Sweden

Figure 1. Synthesis of OER electrocatalyst in alkaline media, consisting of Ex-SnS$_2$ confined Ni(OH)$_2$ and their XRD and Raman characterization. a) Schematic illustration of the synthesis. b) XRD pattern for SnS$_2$ (black) and Ex-SnS$_2$ confined Ni(OH)$_2$ (red). Raman spectra of c) exfoliated Ex-SnS$_2$ (black), Li-Ex-SnS$_2$ (blue), Ex-SnS$_2$ confined Ni(OH)$_2$ (Red), and d) bulk materials Ex-SnS$_2$ (black), Li-Ex-SnS$_2$ (blue), Ex-SnS$_2$ confined Ni(OH)$_2$ (Red).

platform for achieving potent and efficient pre-catalysts in OER and HER systems due to their tunable metal–sulfur coordination environment, excellent electrical conductivity, and remarkable electronic and chemical properties.[14–16] Particularly, cobalt sulfide, nickel sulfide, iron sulfide, copper sulfide, molybdenum sulfide, tungsten sulfide and their composites are promising OER pre-catalysts.[13,17,18] During OER, their surface undergo an in situ electrochemical transformation under anodic oxidation conditions, being irreversibly converted to transition metal (oxy)hydroxides (TMHOs), which are proposed to be the true active species. In this sense, the TMDs are "'pre-catalysts'" rather than "'catalysts'".[19,20] Confining one of the first-row (3d) transition-metal oxides into the van der Waals gaps of these TMDs pre-catalysts endow the system with synergism, and prevents aggregation, thereby guaranteeing the long-term catalytic activity.[21,22] In the family of TMDs, SnS$_2$ possesses large vdW gap ($\approx$0.6 nm), which allows easy intercalation by Li ion and de-intercalation by an active metal oxide substitution.[23] As to the active metal oxide to be confined, it is reasonable to choose based on the track record of first-row (3d) transition-metal oxides in the catalysis of OER. In this regard, Ni and Co species like Ni(OH)$_2$ and Co(OH)$_2$ are widely recognized as excellent water dissociation centers.[24,25] Herein, we report a controllable confinement of Ni(OH)$_2$ nanoparticles into the vdW gaps of layered SnS$_2$ to ensure efficient catalysis in OER. Benefiting from the confinement effect and the in situ reconstruction, the developed catalysts deliver current densities of 50, 100, 250 mA cm^{-2} at overpotentials

of 270, 300, and 420 mV, which fairly compare with the state-of-the-art catalysts. These experimental findings were inspired by theoretical simulations, which gave us a deep understanding of what happens when Ni(OH)$_2$ nanoparticles are confined in the vdW gaps of SnS$_2$. This study offers an opportunity for a profound knowledge on the confinement effect and in situ surface reconstruction during the OER process.

2. Results and Discussion

2.1. Structural Characterization of Nano-Confined Catalyst

A two-step method was followed to confine a transition metal into the vdW gap of layered SnS$_2$, i.e., by intercalating Li$^+$ via dispersing n-butyllithium (n-BuLi) in hexane solution and then exchanging it with Transition Metal (TM). Herein, we intercalate Li$^+$ into the layers of Ex-SnS$_2$ and exchange the Li$^+$ with Ni^{2+} by adding NiCl$_2$·6H$_2$O to the Ex-Li$_x$SnS$_2$ solution, as illustrated in the schematic representation (**Figure 1**a). In this step, the pH of the solution changed from 6.8 to 9.85 indicating the increased alkalinity due to the formation of β-Ni(OH)$_2$ nanoparticles.

To increase the amount of intercalated metal ion in the 2D SnS$_2$, we modified the inter-layer distance and vdW gap of SnS$_2$ by exfoliation under high power ultra-sonication and various exfoliation experiments were conducted until the optimum result was ensured. We varied the sonication time (0 min, 1, 1.5, and 3 h) and checked the amount of Ni atom in the final product.

Accordingly, exfoliation procedure conducted at 1.5 h (Figure S1c, Supporting Information) gives the maximum Ni atom in the final product as corroborated by EDX elemental analysis taken after each exfoliation experiments. To confirm the exfoliation and metal intercalation process, XRD and Raman measurements were performed as illustrated in Figure 1b. All the XRD peaks of the samples can be indexed as the Berndite-2T layered structure of SnS_2 (JCPDS card no. 23–0677, (Figure S1a, Supporting Information)) with an interlayer spacing of 5.90 Å. The shift in peak position in XRD pattern (Figure 1b; Figure S1b, Supporting Information) as well as the peak broadening and the decrease in the intensity of Raman spectra corroborates the widening of the vdW gaps, and the modification of the interlayer spacing of Ex-SnS_2. Then, an easy intercalation of Li^+ and ion exchange between $Li^+ \leftarrow\rightarrow Ni^{2+}$ takes place into the modified vdW gaps of 2D Ex-SnS_2. As can be seen from the (Figure 1b, inset), the (003) diffraction peak at 15.25° in bulk SnS_2 becomes broader and shifts to lower position (15.1°) after $Ni(OH)_2$ nanoparticle confinement in 2D Ex-SnS_2. The intensity of this peak is also diminished after intercalation and exfoliation, suggesting the decrease in particle size and accommodation of more metal ion in the interlayers. However, the XRD patterns meant for the confined $Ni(OH)_2$ NPs are not observed in our result. This may be due to the low crystallinity that is not strong enough to generate detectable signals in the vdW pockets. To identify the phase of the confined materials (α-$Ni(OH)_2$ or β-$Ni(OH)_2$), we synthesized $Ni(OH)_2$ using the same procedure adopted for the production of the sample Ex-SnS_2 confined $Ni(OH)_2$, without adding Ex-SnS_2. Our XRD pattern, as shown in Figure S2c (Supporting Information), reveals that the synthesized $Ni(OH)_2$ is in the β phase. Further, to study the change in structure of the as-synthesized materials (both bulk and exfoliated), Raman spectra were obtained as depicted in Figure 1c,d. Accordingly, bulk SnS_2 displays an intense Raman peak at ≈320 cm^{-1} and a narrow Raman peak feature at ≈200 cm^{-2}, confirming the presence of A_{1g} and E_g modes for 2H-SnS_2, respectively. After exfoliation, the Raman peak for Ex-SnS_2 confined $Ni(OH)_2$ becomes broader as compared to SnS_2 confined $Ni(OH)_2$ due to the decrease in particle size. However, after lithium intercalation, both the bulk and Ex-SnS_2 show three characteristic Raman peaks at 150 cm^{-1} (J1), 218 cm^{-1} (J2), and 334 cm^{-1} (J3). This behavior can be ascribed to the presence of alkali metals like Li: they can donate electrons to SnS_2, making it negatively charged and they can induce phase change, which is stabilized by electrons.[28,29] Nevertheless, the small peak at 150 cm^{-1} (J1) disappeared after cation exchange Li→Ni. This is an expected behavior because the transition metals like Ni reduce electron donating ability in the surrounding.

To study the surface morphology, SEM and TEM were used. The SEM images in Figure S3a,b (Supporting Information) show that the exfoliation process downsizes the SnS_2 nanosheets into nanoflakes. The high-resolution TEM (HR-TEM) image in **Figure 2** clearly shows the lattice fringes recorded with well-defined lattice space for both pristine SnS_2 and Ex-SnS_2 nanosheets confined $Ni(OH)_2$ nanoparticles. Moreover, from Figure 2b,c the broader and disordered feature of the basal planes of Ex-SnS_2 is evident after $Ni(OH)_2$ confinement, as compared to bulk SnS_2 (Figure 2a). This confirms the intercalation and confinement of $Ni(OH)_2$ into the layers of Ex-SnS_2. The 0.57 nm d-spacing for (001) plane in our HRTEM result (Figure 2b) confirms that the

formed $Ni(OH)_2$ is β-$Ni(OH)_2$ phase, in agreement with XRD data on $Ni(OH)_2$ particles. Interestingly, the confinement process induced the formation of defects and/or dislocations on the material. This degree of disorder in 2D materials increases the density of active sites, and retains electron transport along basal surfaces, which in turn gives good catalytic performance.[13] The corresponding selected area electron diffraction (SAED, Figure 2d) patterns for the confined surface expectedly contains (101) and (100) planes of $Ni(OH)_2$, and (001) and (011) planes of Ex-SnS_2. To gain additional information on the composition and elemental distribution, energy dispersive spectroscopy (EDS) elemental mapping connected to scanning TEM (STEM) (Figure 2e) and SEM (Figure S3c–e, Supporting Information) were applied. The Sn, S, Ni, and O elements are uniformly distributed in the synthesized material. The HRTEM, STEM, and EDS results suggest that $Ni(OH)_2$ nanoparticles are confined into the interlayer spaces of the Ex-SnS_2 Nanosheets.

To gain insight into the surface chemistry, the chemical composition, and the oxidation states of the samples, we performed X-ray photoelectron spectroscopy (XPS). In the Ni 2p spectra (**Figure 3**a), 2p3/2 (856.2 eV) and 2p1/2 (874.3 eV) peaks were assigned to the Ni^{2+} in $Ni(OH)_2$. There is a noticeable difference in the BE of Ni in the confined $Ni(OH)_2$ and that of unconfined $Ni(OH)_2$. We have particularly measured a 0.3 eV difference of the main Ni^{2+} XPS peaks from Ex-SnS_2 confined $Ni(OH)_2$ (857.0 eV) and pristine $Ni(OH)_2$ (857.3 eV) substantiating a remarkable charge transfer between Sn^{4+} and Ni^{2+}.[30,31] Similarly, the surface chemical states of Sn were also investigated. The XPS Sn 3d peaks located at the BE of 486.7 and 495.1 eV are assigned to 3d5/2 and 3d3/2 of Sn (Figure 3b). They reveal that the valence state of Sn is +4. The broadening of the doublet peak in the confined material could be ascribed to the higher disorder of the system after $Ni(OH)_2$ confinement. The XPS S 2p spectra of SnS_2 show the S^{2-} doublet at 162.3 and 163.7 eV (Figure 3b). The XPS S 2p spectra of Ex-SnS_2 confined $Ni(OH)_2$ show an additional peak at higher binding energy (168.6 eV), which corresponds to the existence of an S−O bond and formation of hydroxide species at higher pH. The broader XPS S 2p peak of Ex-SnS_2 confined $Ni(OH)_2$ compared to that of SnS_2 reveals various sulfur bonding. Likewise, the chemical nature and existence of oxygen and hydroxide ion (OH$^-$) is deemed from the collected XPS spectra, as shown in Figure 3c. This result is also consistent with previous works.[32,33] Thus, the XPS O 1s spectra of $Ni(OH)_2$ and Ex-SnS_2 confined $Ni(OH)_2$ display two de-convoluted peaks centered at 531.6 and 530.5 eV (Figure 3d), corresponding to oxygen ions (O lattice) and oxide species, respectively. Figure S4 (Supporting Information) shows the survey XPS spectra of the $Ni(OH)_2$, SnS_2 and Ex-SnS_2 confined $Ni(OH)_2$ that confirm the co-existence of the S 2p, Ni 2P, Sn 3d at their respective binding energy, in agreement with the expected composition.

2.2. Insight into the Water Oxidation on Ex-SnS_2 Confined $Ni(OH)_2$

At first, the surface electrochemical properties of Ex-SnS_2 confined $Ni(OH)_2$ were studied to understand the reaction types at various applied voltages. To this end, cyclic voltammetry (CV) was run. As expected, during the electrocatalytic water oxidation by
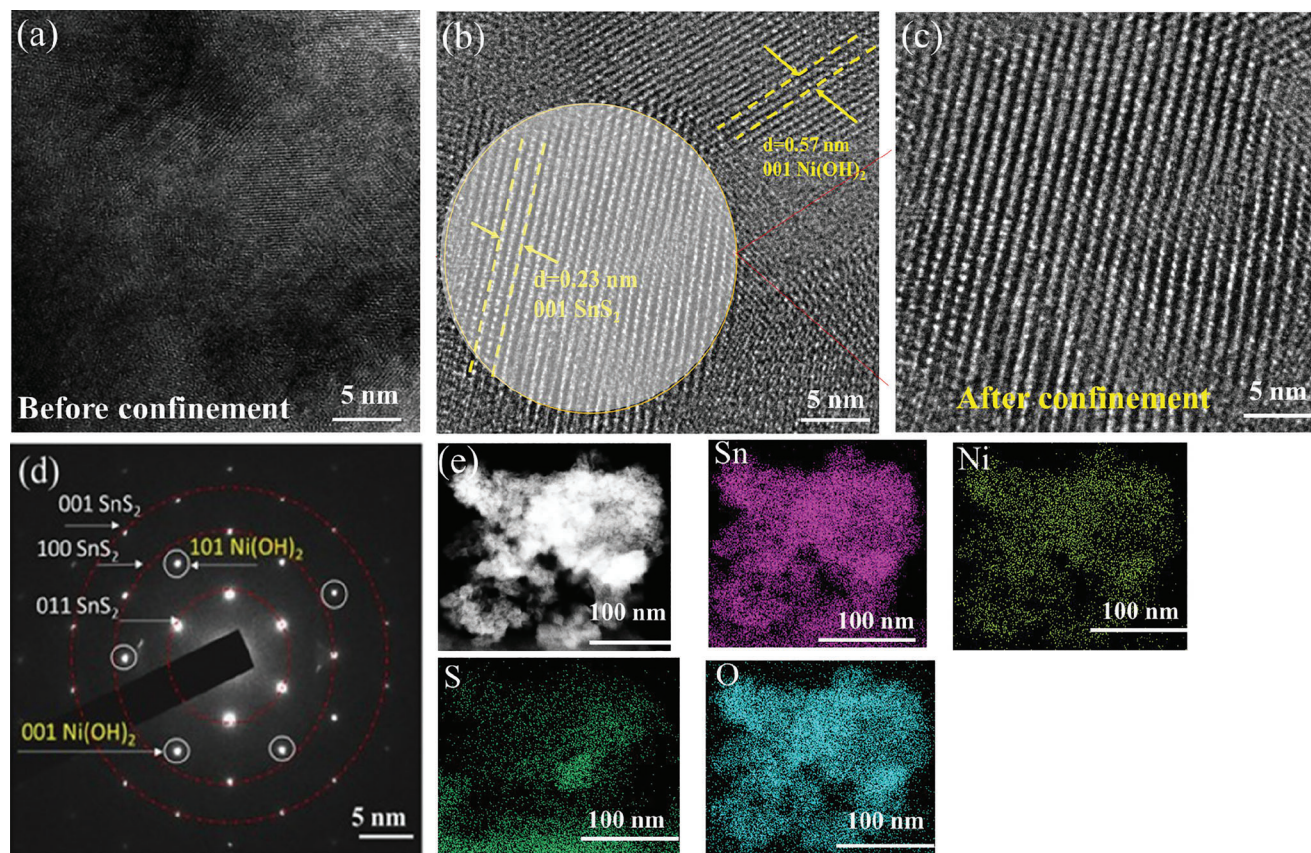
**ADVANCED
SCIENCE NEWS**

www.advancedsciencenews.com

**small
methods**

www.small-methods.com

Figure 2. HRTEM image of a) Ex-SnS$_2$, b) Ex-SnS$_2$ confined Ni(OH)$_2$, and c) magnified area of Ex-SnS$_2$ in Ex-SnS$_2$ confined Ni(OH)$_2$. d) SAED patterns of Ex-SnS$_2$ confined Ni(OH)$_2$. e) STEM image and elemental mapping for Sn, Ni, S, and O in Ex-SnS$_2$ confined Ni(OH)$_2$.

nickel based catalysts, one common process attributable to the Ni^{2+} ↔ Ni$^{3/4+}$ peak (**Figure 4**a) was detected in the CV plots. This redox process happens together with the formation of the O*, which is an essential intermediate (coupling with one OH$^-$ group to generate *OOH) for oxygen evolution.[34,35] Basically, the OER begins with the adsorption and discharge of OH$^-$ at catalyst surface and gives rise to the formation of adsorbed OH species (OH*) [* + OH$^-$ → OH* + e$^-$]. Then, the produced surface OH* can further react with OH$^-$ in the electrolyte, resulting in the formation of H$_2$O and adsorbed atomic O (O*) [OH* + OH$^-$ → O* + H$_2$O + e$^-$]. Third, the surface O* combines with OH$^-$ and forms adsorbed OOH species (OOH*) [O* + OH$^-$ → OOH* + e$^-$], and the additional OH$^-$ reacts with the OOH* leading to the formation of adsorbed O$_2$ and H$_2$O [OOH* + OH$^-$→* + O$_2$ + H$_2$O + e$^-$].[36] Electrochemically, these reaction intermediates occur in three different potential regions: at the low potential (region ①), *OH generation; in the mid potential (region ②), metal redox transition; then, O$_2$ will be generated under high potential (region ③, water oxidation regions). The three simplified processes of water oxidation involve the *OH species adsorption, *O radical formation, and *OOH transformation and desorption.[37] Specifically, these categories can be considered as pre-catalytic stage also called metal oxidation stage, catalytic OER stage, and post OER stage. In the pre-catalytic stage, de-protonation (*Ni−O-H-O-H→ *Ni^{3+}-O +H$_2$O) and structural transformation from hydroxides into oxyhydroxides in (Ni(OH)$_2$→ NiOOH, which is the OER ac-

tive site) takes place. Likewise, in catalytic OER stage, Ni^{3+}−O * + 2OH → Ni^{3+}−O * + O$_2$ is formed.[24,38] The result from CV study confirms that the confined Ni(OH)$_2$ is transformed to NiOOH in the second stage of OER process, suggesting the formation of a new active component in the confined environment. In this sense, the synthesized material is just a pre-catalyst delivering the true catalyst containing NiOOH via electrochemical activation.

2.3. Electrocatalytic Water Oxidation Performance

The activity of the electrochemically induced catalyst was measured in O$_2$-saturated 1 м KOH solution by using a conventional three-electrode configuration where a Ag/AgCl$_2$ (reference), a graphite rod (counter), and the samples under investigation (working electrodes) were applied. The polarization curves of SnS$_2$, Li-Ex-SnS$_2$ and Ni(OH)$_2$ depicted in Figure S5a (Supporting Information) display only modest activity toward OER. In any way, to avoid the effect of capacitive current originating from the Ni ion oxidation on the catalytic performance, LSV with reverse scan was measured for the OER performance test as can be seen in Figure 4b. As expected, the Ex-SnS$_2$ confined Ni(OH)$_2$ exhibited substantially higher catalytic activity with an onset overpotential of 180 mV. The Ni(OH)$_2$ delivers current density of 10, 100, and 250 mA cm^{-2} at a potential of 1.60, 1.70, and 1.85 V versus RHE, respectively, far beyond those of the counterpart
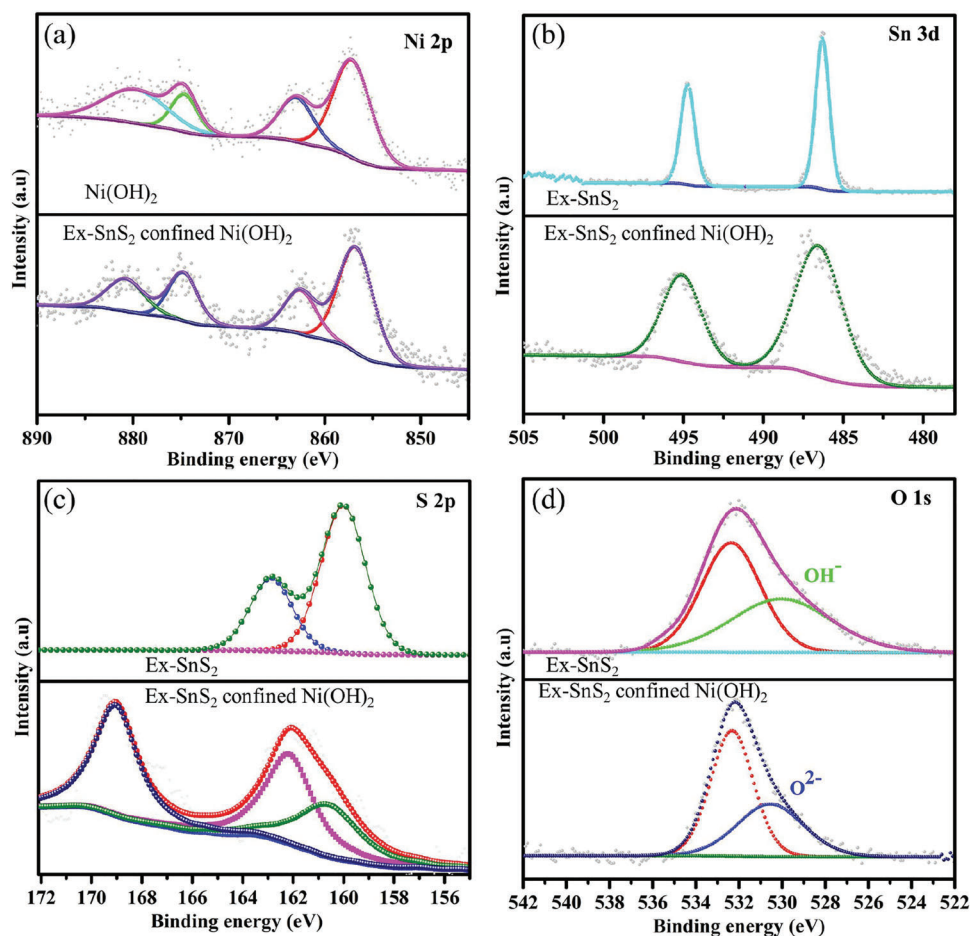
Figure 3. High-resolution XPS a) Ni 2p spectra of Ni(OH)$_2$ and Ex-SnS$_2$ confined Ni(OH)$_2$, b) XPS Sn 3d spectra of SnS$_2$ and Ex-SnS$_2$ confined Ni(OH)$_2$, and c) XPS S 2p spectra of SnS$_2$ and Ex-SnS$_2$ confined Ni(OH)$_2$, and d) XPS O 2p spectra of in Ni(OH)$_2$ and Ex-SnS$_2$ confined Ni(OH)$_2$.

samples and compared with the best OER electrocatalysts reported by far (Table S1, Supporting Information). Benefiting from these features, Ex-SnS$_2$ confined Ni(OH)$_2$ delivers current density of 10, 100, and 250 mA cm^{-2} at a potential of 1.55, 1.65, and 1.78 V versus RHE, respectively. However, the redox reaction associated to Ni^{2+} and Ni^{3+}/ Ni^{4+} develops a capacitive current and hence impairs the direct measurement of the performance of the catalyst pertinent to OER. This redox reaction is recognized from the prominent peak in the LSV curve, typical of Ni based materials. In our case, this oxidation peak for Ex-SnS$_2$ confined Ni(OH)$_2$ appears at lower anodic peak than the pure Ni(OH)$_2$. This is due to the higher 3d electron density that is induced by the electron flow between the Ex-SnS$_2$ and Ni(OH)$_2$, which possibly suppresses the electrochemical oxidation of Ni(OH)$_2$ in the confined material.

To confirm that the interface confinement is beneficial to increase the activity of the materials, electrochemically active surface area (ECSAs) of catalysts was calculated based on the proportional relationship with double-layer capacitance (C$_{dl}$) values and ECSAs (**Figure 5**c; Figure S4a,b, Supporting Information). In this framework, the C$_{dl}$ was estimated by measuring the cyclic voltammetries at different scan rates in a non-faradic region.[4] As a re-

sult, the C$_{dl}$ value of Ex-SnS$_2$ confined Ni(OH)$_2$ (11.3 mF cm^{-2}) is found to be higher than that of Ni(OH)$_2$ (10.8 mF cm^{-2}). As one member of the layered metal dichalcogenides family, the basal planes of pristine SnS$_2$ exhibit poor activity and limited exposure of active sites in catalysis. It is expected that most of the surface oxygen functional groups are attached on the edge planes. This study focuses on improving the catalytic activity of SnS$_2$ on the basal plane in addition the edge. We believe that the confined Ni(OH)$_2$ into the vdW gaps of Ex-SnS$_2$ result in introducing another catalytically active site in the confined pocket. Therefore, whereas the active sites on the edge may also contribute to the OER, the new catalysts in the confined environment (together with the associated defects) most evidently play a more pronounced role than in the case of the bulk SnS$_2$. This result demonstrates that the surface confinement obviously triggers the exposure of more active sites on the surface, which can significantly enhance the intrinsic activity. To further understand the OER kinetics, Tafel slopes were extracted from the polarization curves. The Ex-SnS$_2$ confined Ni(OH)$_2$ exhibits a Tafel slope of 93 mV dec^{-1}, much lower than the Ni(OH)$_2$ (106 mV dec^{-1}) (Figure 4d). The lower Tafel slope suggests the faster reaction kinetics for oxygen evolution and rapid electron transfer in the
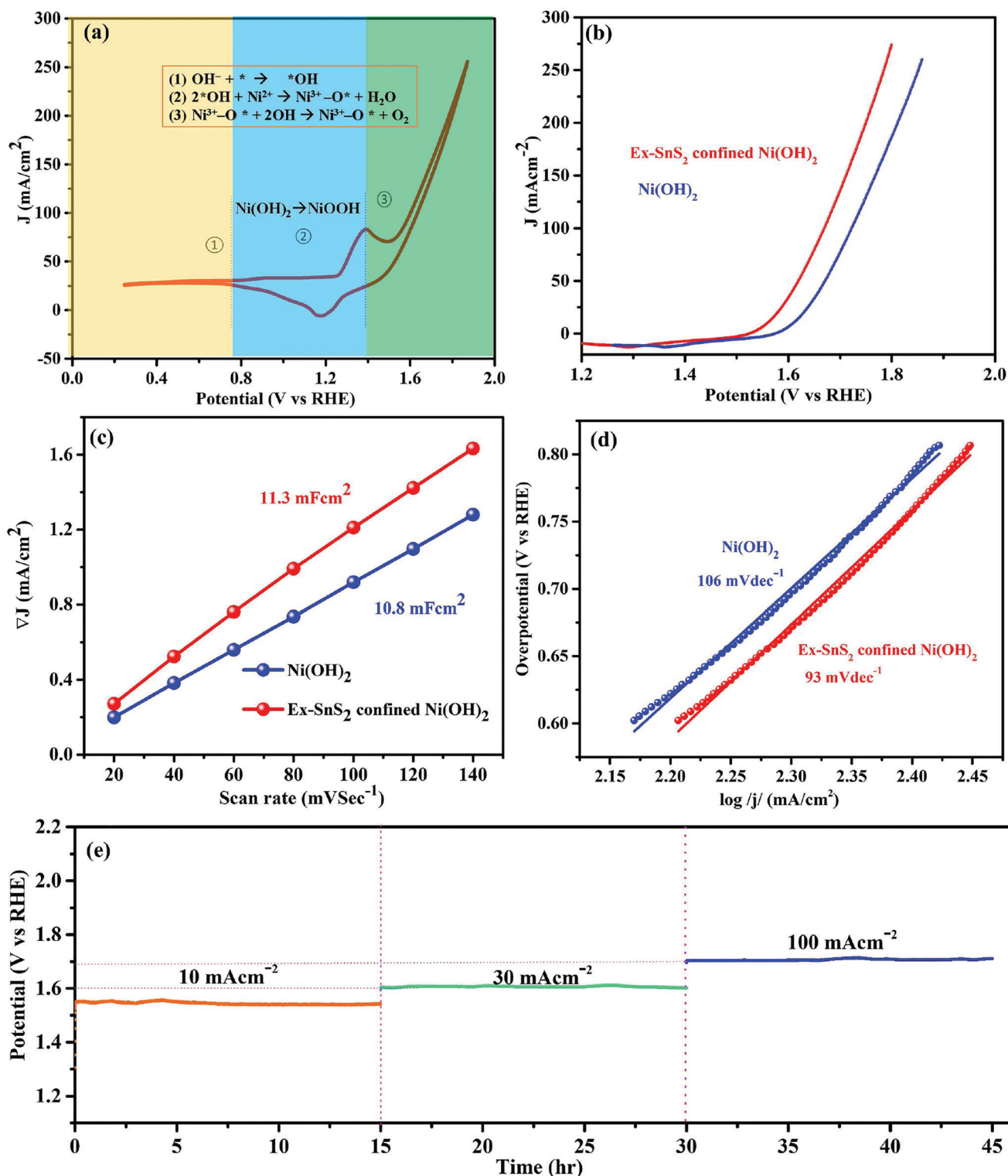
Figure 4. Electrochemical analysis of Ex-SnS$_2$ confined Ni(OH)$_2$ for OER processes. a) Cyclic voltammetry. b) Reverse scan OER polarization curves from the linear sweep voltammetry. c) Double-layer capacitance (C$_{dl}$) measurements of Ex-SnS$_2$ confined Ni(OH)$_2$ and Ni(OH)$_2$ catalysts. d) Tafel plots of pristine Ni(OH)$_2$ catalysts and Ex-SnS$_2$ confined Ni(OH)$_2$. e) Chronopotentiometric run of Ex-SnS$_2$ confined Ni(OH)$_2$ for the long-term durability test at 10, 30, and 100 mA cm^{-2}.

ADVANCED
SCIENCE NEWS
www.advancedsciencenews.com
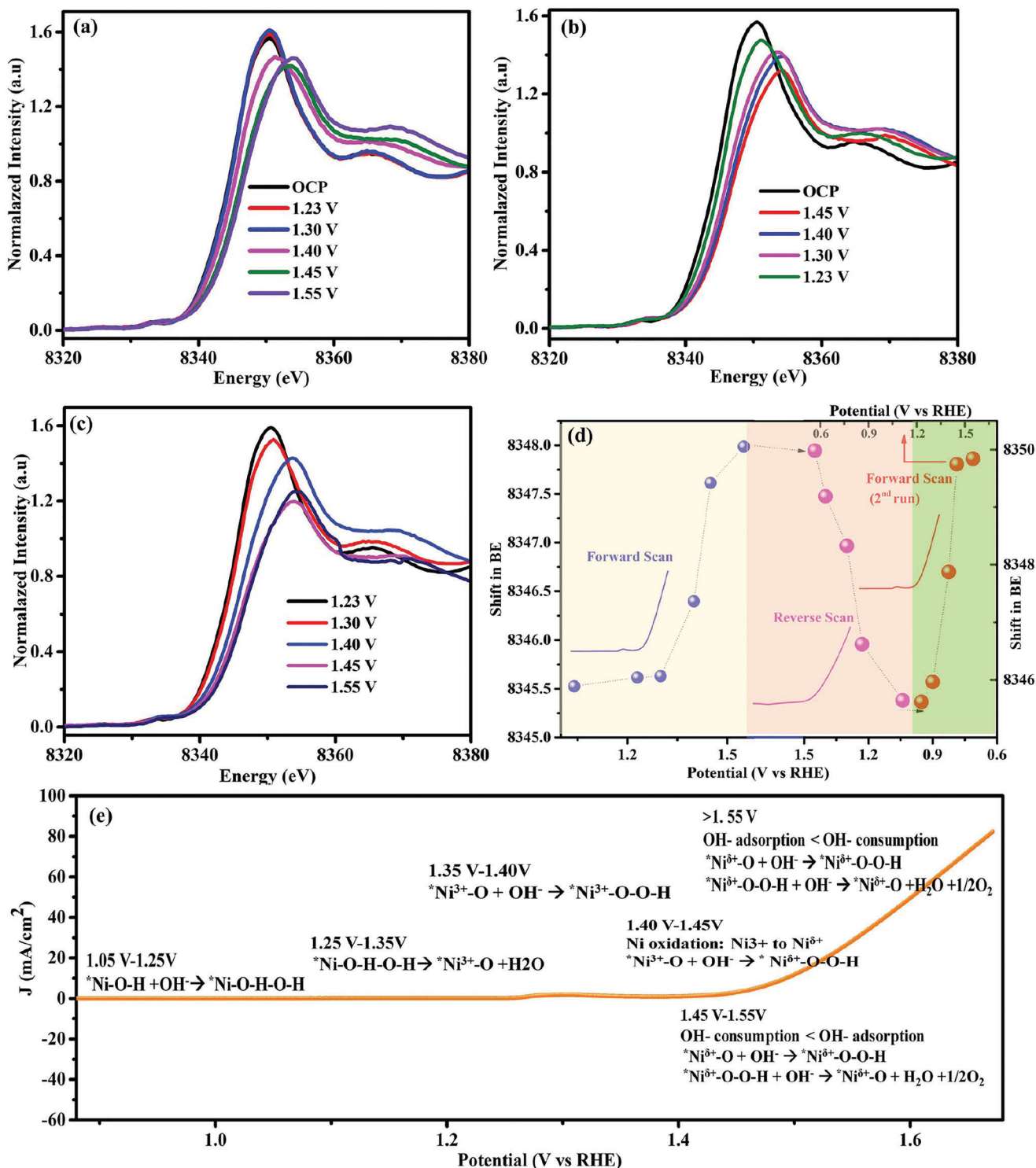
small
methods
www.small-methods.com

Figure 5. Electrochemically controlled in situ Ni K-edge XANES for Ex-SnS$_2$ confined Ni(OH)$_2$ collected under different a) forward scan polarization potentials, b) reverse scan polarization potentials, and c) 2nd run forward polarization potentials. d) Ni K-edge energy shift of Ex-SnS$_2$ confined Ni(OH)$_2$. e) OER reaction intermediates and corresponding electrochemical potentials.

confinement. Furthermore, OER catalyst stability is a bottleneck in realizing scalable water-splitting technology. We performed chronopotentiometry at 10, 30, and 100 mA cm^{-2} current densities for a total of 45 h (15 at each current density). As can be seen from Figure 4e, Ex-SnS$_2$ confined Ni(OH)$_2$ retains 99.99% of the activity at all current densities. This is due to the "sandwich" structure resulting from the confinement, which avoids the aggregation or loss that could happen in free space, and facilitates easy mass transfer in this catalytic system.[39]

2.4. In Situ XAS Probed Electronic Structure of Ex-SnS$_2$ Confined Ni(OH)$_2$ Nanoparticles

To understand the local electronic state, and the coordination environment of the pre-catalyst and in situ generated catalyst, in situ XAS spectra were collected. With this method, we probed the change in oxidation state and the structural stability during OER catalysis at various applied potentials. We performed a forward LSV run while measuring the XAS spectra to observe the change in oxidation state of Ni atom during catalysis. We further cross-checked the reversibility of this phenomenon by repeating the same XAS measurement under reverse LSV scan. In the case of the forward run, as depicted in Figure 5a, the very small peaks in the range of the pre-edge at (8.325 to 8.335 KeV) in Ni K-edge imply that the octahedral atom arrangement is predominant as in the form of Ni(OH)$_2$ species. Likewise, the white line of Ni K-edge shifts to higher energy during the 1st forward LSV scan, when the potential changes from OCP to 1.55 V, confirming the deprotonation and oxidation of Ni(OH)$_2$ to NiOOH species. Specifically, upon the increase of polarization potentials, the shift toward higher energy of the Ni K-edge implies the increment of the oxidation state of from Ni^{2+} to Ni$^{3/4+}$. In the potential range from OCP to 1.23 V, mainly *Ni-O-H + OH$^-$ → *Ni-O-H-O-H is formed.[24] The small positive shift of the white line in 1.3 V compared to OCV and 1.23 V, confirms that the slight oxidation of Ni starts at 1.3 V. In the range 1.3–1.40 V, where the metal oxidation peak appears in the LSV, the transformation from Ni^{2+} to Ni^{3+} takes place. At this stage, the protons on the hydroxyls of Ex-SnS$_2$ confined Ni(OH)$_2$ are partially decoupled. Thereafter, the Ni^{3+} begins to be slowly oxidized at 1.40 V toward a higher oxidation state, where the OER is still not yet activated. With the further increase in the applied potential to 1.45 V, where the apparent OER is already started, the valence state of Ni reaches a higher state, indicating that the pre-catalyst is transformed into the real active OER catalyst (i.e NiOOH). However, the Ni K-edge XANES spectra at 1.45 and 1.55 V almost coincide, indicating that the transformation to Ni^{2+} was already finished at 1.45 V. As to the case of the reverse scan, **Figure 6**b indicates that the oxidation states of Ni are back to their original position. The observation from both reverse and forward scan in situ measurements serve as a solid proof that the de-protonation reaction of the as-synthesized catalyst is potential dependent and shows good electrochemical reversibility. Moreover, to gain a deeper understanding on the material's structural stability during electrochemical measurements, we further measured the forward LSV scan for the second time and recorded the in situ XAS data (2nd forward LSV run). From Figure 6b, it is clear that the trend is similar to the first forward LSV run. This suggests an excellent structural stabil-

ity, in addition to the redox reversibility, at the surface of the catalyst. Further, the energy shifts (E−E$_0$) in Ni K-edge XANES spectra was plotted as a function of potential (Figure 5d). The absorption energy of white line position was defined over the half height of the normalized edge height. The variation in oxidation state during the 1st run (both forward and reverse LSV scan) and the 2nd run forward LSV scan, and the corresponding electrochemical behaviors with its possible reaction mechanisms are depicted in Figure 5e. For a comparison purpose, we measured the in situ XAS for the un-confined Ni(OH)$_2$ as shown in Figure S6b (Supporting Information). It is evident that the oxidation state of Ni in the un-confined Ni(OH)$_2$ takes place relatively slowly as compared to the one in the case of confined Ni(OH)$_2$. This explains the reason behind the sluggish kinetics observed from the Tafel plot in Figure 4d for unconfined Ni(OH)$_2$. The corresponding I-t curve of Ex-SnS$_2$ confined Ni(OH)$_2$ used for collecting the in situ XAS data is also illustrated in Figure S7a–c (Supporting Information).

Concurrently, details about the local environment and the average bond length of neighboring atoms can be acquired from EX-AFS spectra.[37] The Ni K-edge EXAFS spectra display two main peaks at 1.5 Å, which are attributed to six-equidistant oxygens around Ni, i.e., Ni−O, and at 2.6 Å the Ni−M derived from the contribution of Ni−Ni and Ni−Sn shells scattering. The Ni−O and Ni−M distances of 1.5 and 2.6 Å prevailing at 1.23 V correspond to Ni(OH)$_2$ phase.[40] According to the fitting results of in situ Ni K-edge EXAFS spectra (Figure S7d; Table S2, Supporting Information), we found that the distances of Ni−O and Ni−Ni/Sn undergo a significant change. In situ Ni K-edge k^2-weighted FT spectra of Ex-SnS$_2$ confined Ni(OH)$_2$ show that the coordination number and bond length of Ex-SnS$_2$ confined Ni(OH)$_2$ were altered successively with the applied potentials. Hence, the intensity of both Ni−O and Ni−M shells gradually decreases with the increase in applied potentials, because of the phase formation existing in the different environments, due to the occurrence of redox transition from Ni(OH)$_2$ to NiOOH. Like the white line shift, the Ni−O peaks under forward polarization potentials (Figure 6a) show variation in bond length of Ni−O and Ni−Ni and contract step by step with the increment of polarization potentials from OCP to 1.55 V. Meanwhile, the Ni−O bond (1.44 Å) in the confined material is decreased, as compared to the Ni−O bond (1.46 Å) in un-confined Ni(OH)$_2$ (Figure S6c, Supporting Information), which might be attributed to the formation of Ni$^{3+/4+}$ species during OER.[41] In comparison with the pristine one (without electrolytes, Figure S6c, Supporting Information), the increase in peak intensity in Ex-SnS$_2$ confined Ni(OH)$_2$ relative to OCP, confirms the increased coordination number (CN) of Ni−O with the intercalation of a large number of OH$^-$ into the interlayer space. Compared to OCP, the decrease in CN at 1.23 V from 6.00 to 5.08 is due to the vacancy formation. As the applied potential increases from 1.23 to 1.30 V, the protons on hydroxyls decouple and recombine with the adsorbed OH$^-$ to form H$_2$O. Thus, the coordination number around Ni decreases the electrochemical adsorption of OH$^-$ again in the potential range of 1.30 to 1.40 V. As the potential further increase from 1.40 to 1.45 V, Ni^{3+} is further oxidized to the higher valence state. The Ni−O pairs with d$_{Ni−O}$ of 1.38 Å and Ni-metal pairs with d$_{Ni−M}$ of 2.45 Å at 1.45 V. The gradual decrement in bond length with the increment of the applied potentials suggests the formation of
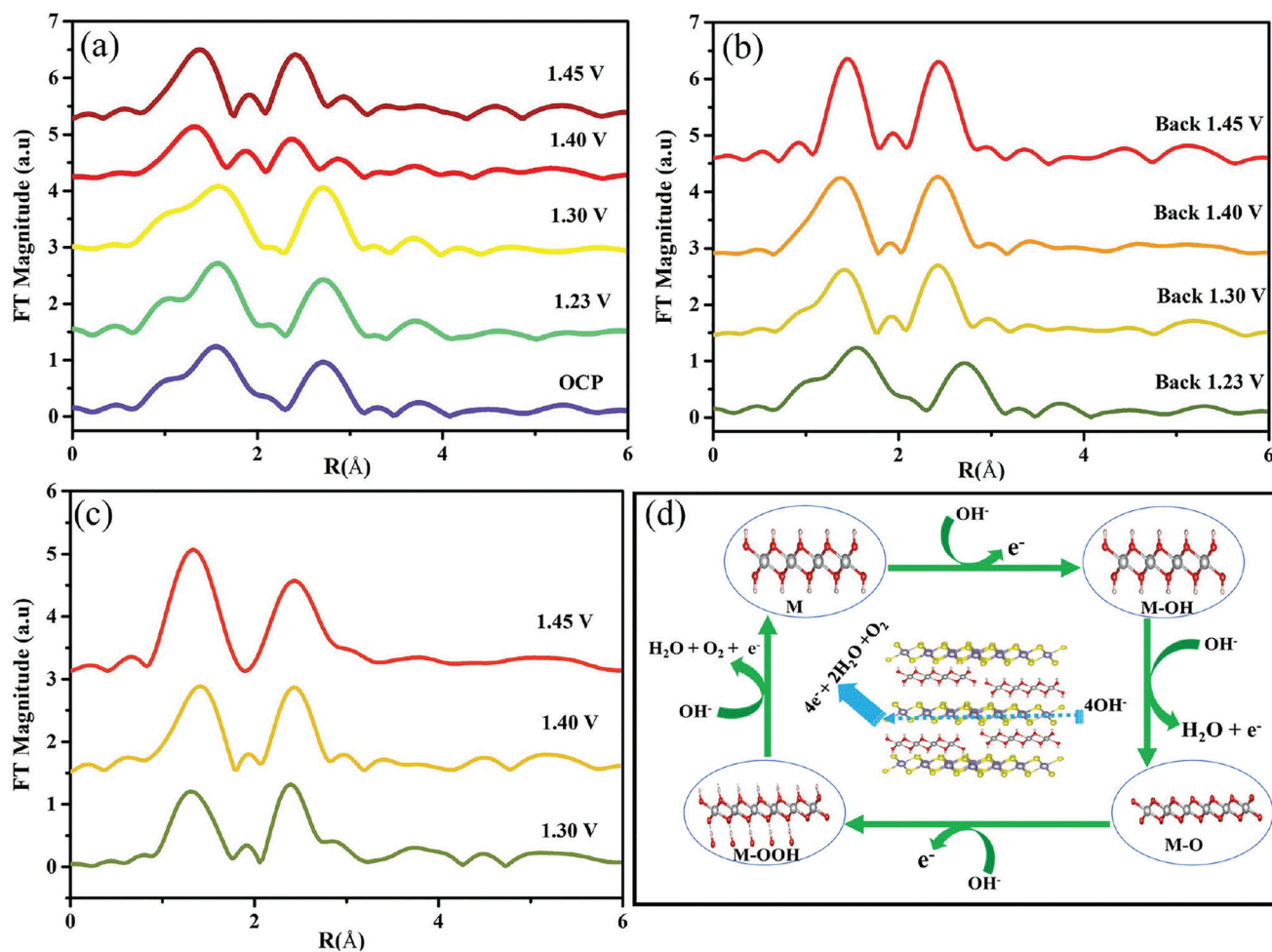
**ADVANCED
SCIENCE NEWS**

www.advancedsciencenews.com

**small
methods**

www.small-methods.com

Figure 6. In situ Ni K-edge k^2-weighted FT spectra of Ex-SnS$_2$ confined Ni(OH)$_2$ collected under a) forward polarization potentials, b) back polarization potentials, and c) 2nd run forward polarization potentials. d) The schematic illustration of the OER reaction mechanism on the surface of Ex-SnS$_2$ confined Ni(OH)$_2$ nanoparticle (M stands for Ni Metal). The OER mechanism possibly involves the formation of NiOOH intermediate species.

new phases, existing in the different environments due to the occurrence of redox transition from Ni(OH)$_2$ to NiOOH. Similarly, excess OH$^-$ on the surface of active Ex-SnS$_2$ confined Ni(OH)$_2$ accumulates.[42] These peaks reversibly shift back to lower energy upon reverse scan, as shown in Figure 6b. This increase in CN comes from the electrochemical adsorption of OH$^-$ on the surface of confined Ni(OH)$_2$, as the increasing coordination number of Ni–O promotes the multiple scattering in Ni–O coordination geometry. This suggests that the redox pair reactions (either a two-step reaction of Ni^{2+}/Ni^{3+} and then Ni^{3+}/Ni^{4+}, or a one-step reaction of Ni^{2+}/Ni^{4+}) might take place during forward and reverse OER scan. Similar to XANES spectra of Ex-SnS$_2$ confined Ni(OH)$_2$ catalysts, we also measured the EXAFS spectra of Ex-SnS$_2$ confined Ni(OH)$_2$ catalysts during the 2nd run forward scan (Figure 6c) for the confirmation of the materials structural stability during electrochemical measurement. As a result, the confined Ni(OH)$_2$ fully oxidizes to higher oxidation state of Ni, suggesting that the "sandwich" structure of the Ex-SnS$_2$ confined Ni(OH)$_2$ keeps the material stability of Ni(OH)$_2$. The shortening of both Ni–O and Ni–M bonds suggests that the crystal structure of Ni(OH)$_2$ underwent dynamic changes during OER reaction to

NiOOH. Based on the above results, herein we summarize the OER reaction mechanism on Ex-SnS$_2$ confined Ni(OH)$_2$ catalyst, as shown in Figure 6d.

To unlock the key understanding of the source of the real catalytic activity, we characterized the crystal structure (XRD), the electronic state/chemical environment (XAS/EXAFS) and the morphology (FE-SEM) of the sample after OER.[43] Post-OER XRD characterizations were conducted to understand the crystal structure and electronic state changes during the catalytic reaction. This result shows the advent of new peaks (as compared to **Figure 7**a) meant for SnO$_2$ in addition to SnS$_2$. We believe that the newly induced oxide phases synergize with the existing parent phase that results in the true catalyst. Such electrochemically induced oxides/hydroxides apparently perform better in catalysis as compared to pristine oxide (un-confined Ni(OH)$_2$). This is due to the synergism and enhanced conductivity as reported in another literature as well.[44] From the EDS elemental mapping (Figure 7b–e) we can see the presence and consistent distribution of Ni, Sn, and S across the entire surface of the nanosheet. To further approve the change in oxidation state and electronic properties, post OER XANES and EXAFS measurements were
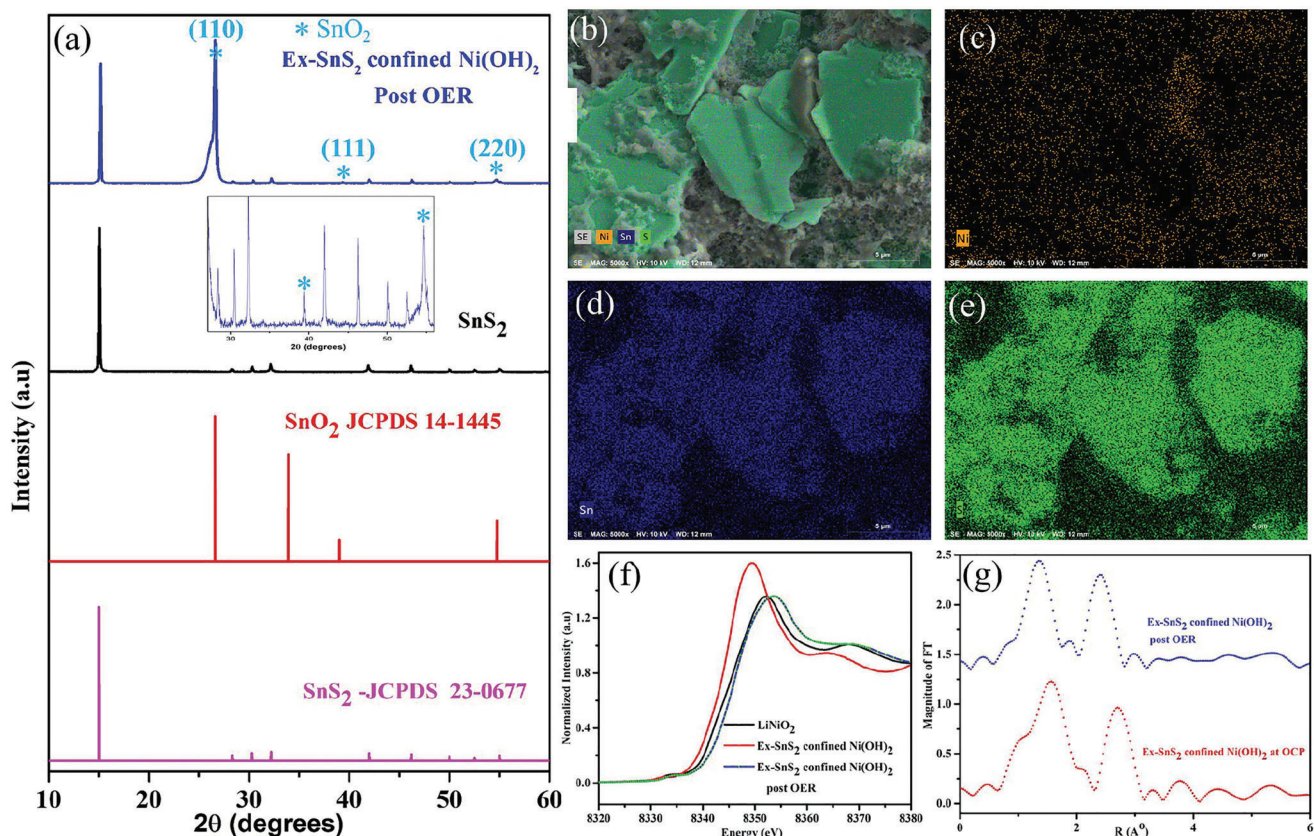
**ADVANCED
SCIENCE NEWS**

www.advancedsciencenews.com

**small
methods**

www.small-methods.com

Figure 7. Post OER characterizations: a) XRD, b) SEM, relative EDS mapping for c)Ni, d) Sn, and e) S. f) XANES and g) Ni *K*-edge k^2-weighted FT spectra of Ex-SnS$_2$ confined Ni(OH)$_2$.

performed. As a result, the Ni *K*-edge XANES spectrum (Figure 7f) of the Ex-SnS$_2$ confined Ni(OH)$_2$ nanoparticle sample before OER is very similar to the XANES spectrum of the Ni(OH)$_2$ sample, exhibiting the Ni oxidation state of +2. After OER, the XANES spectrum of Ex-SnS$_2$ confined Ni(OH)$_2$ nanoparticles coincides to that of LiNiO$_2$, because the surface oxidized and the Ni oxidation state lay above two. The Ni EX-AFS spectra of Ex-SnS$_2$ confined Ni(OH)$_2$ nanoparticle before and post OER (Figure 7g) display Ni–O, and Ni–M (M = Ni, Sn) shells. Accordingly, the positions of the Ni–O (1.5 Å) and Ni–M (2.7 Å) shells gradually decrease to Ni–O (1.35 Å) and Ni–M (2.4 Å) after OER, suggesting the formation of new phases existing in the different environments due to the occurrence of redox transition of Ni(OH)$_2$ to NiOOH. In this case, the SnS$_2$ undergo an in situ electrochemical transformation under anodic oxidation conditions, being irreversibly converted to transition metal (oxy)hydroxides (TMHOs), which are proposed to synergize with the NiOOH and to act as the true catalyst for OER.

3. Conclusion

In summary, we presented a facile confinement procedure for efficient water oxidation pre-catalyst under alkaline medium. To confirm the confinement, HRTEM, XRD, Raman, EDS, and XPS analyses were used. By using Ex-SnS$_2$ as a pre-catalyst, the in situ

generated and confined Ni(OH)$_2$ catalyst delivered outstanding OER activity with current density of 100 mA cm^{-2} at an overpotential as low as (300 ± 5) mV versus RHE and excellent cycling stability without potential drop for 45 h at current densities of 10, 30, and 100 mA cm^{-2}. The excellent cycling stability is due to the "sandwich" structure of the Ex-SnS$_2$ confined Ni(OH)$_2$, which avoids the aggregating or the falling out of Ni(OH)$_2$, and that facilitates the easy mass transfer in this catalytic system. Herein, we combine electrochemical measurements and in situ XAS to elucidate the catalytically active phase, the reaction center and the OER mechanism. The XAS analysis shows that Ni(OH)$_2$ and Ex-SnS$_2$ play co-joint roles for the outstanding OER performance. In addition to the improved activity, the Ni(OH)$_2$ "promoters" confined in the 2D Ex-SnS$_2$ nanosheets are protected from aggregation or losses that could happen in free space, leading to the improved cycling stability of the confined catalyst. This work shows that the confined material as pre-catalyst and the in situ-formed hydroxide and oxyhydroxide moieties play an active role in catalysis, in which the sulfide vicinity also contributes its part. Moreover, the oxygen-bound intermediates interact more favorably on the Ex-SnS$_2$ confined Ni(OH)$_2$ surface as compared to the pristine Ni(OH)$_2$ ones, which can contribute to the enhanced OER catalysis. This study demonstrates the prominent role of confinement as pre-catalyst in water splitting and paves the way for the subsequent investigations in the quest for breakthroughs in many energy conversion and storage techniques.

4. Experimental Section

Synthesis of 2D Exfoliated SnS₂ Confined Ni(OH)₂ Electrocatalyst: The Ex-SnS₂ confined Ni(OH)₂ was synthesized by a two-step method. The first step was the preparation of Li-intercalated commercial SnS₂ nanosheets. SnS₂ nanosheets (1 g), obtained by exfoliation (named as Ex-SnS₂ here after), were dispersed in n-BuLi/ hexane solution (15 mL, 2 M) in an argon filled glovebox, and stirred at room temperature for two days. The black product obtained was then washed repeatedly with anhydrous hexane and then centrifuged (8000 rpm for 30 min) to remove excess n-BuLi and other soluble impurities. The second step is the ion exchange of Li$^+$ by Ni^{2+} in an alkaline environment to form SnS₂ nanosheets intercalated with Ni(OH)₂. To achieve this, NiCl₂·6H₂O, and anhydrous NMP (18 mL) were added to a Teflon autoclave containing estimated amount of Ex-SnS₂ obtained in the first step. After stirring the mixture in a glovebox to form a homogeneous suspension, it was sealed in the autoclave and underwent a solvothermal process at 80 °C for 48 h. The pH values of the suspension were 6.8 and ≈9.85, before and after the reaction, indicating the generation of OH$^-$ during the reaction of lithium with water in NiCl₂·6H₂O upon heating. The product was then washed thoroughly with four different solvents (NMP, isopropanol, ethanol, and water) before being dried in a freeze-dryer. The obtained sample was denoted Ex-SnS₂ confined Ni(OH)₂. For the synthesis of SnS₂ confined Ni(OH)₂, bulk SnS₂ powder was used instead of Ex-SnS₂ Nanosheets, while all the other steps were the same. For comparison purpose, un-confined Ni(OH)₂ was also synthesized according to the synthesis procedure described in Supporting Information.

Material Characterization Techniques: X-ray diffraction (XRD) using a Bruker D2 Phase XRD diffractometer, equipped with a Cu-Kα irradiation photon source (λ = 1.5406 Å, Ni filter, 30 kV and 10 mA) was applied to characterize the crystal structure of the samples. The surface morphology and elemental composition were determined by field emission scanning electron microscopy (FESEM; JEOL 6700F) equipped with an energy-dispersive X-ray spectrometer (EDS; Inca Energy 400). High-resolution transmission electron microscopy (HRTEM; JEOL JEM-2100F) and energy-dispersive X-ray spectroscopy (EDS; OXFORD X-Max) were conducted to investigate the crystal structure and the elemental compositions, respectively. The Raman spectra were obtained using a Jobin-Yvon Lab RAM HR800 system with a laser source of 532 nm. High-resolution XPS spectra were acquired at the VG Scientific ESCALAB 250 (NTU, Taiwan).

In Situ X-Ray Absorption Spectroscopy (XAS): In situ X-ray absorption spectroscopy (XAS) measurements were performed at the TLS 17C and 01C1 beamlines in National Synchrotron Research Radiation Center (NSRRC). The in situ X-ray absorption spectra, including X-ray Absorption Near Edge Fine Structure (XANES) and Extended X-ray Absorption Fine Structure (EXAFS), were collected for the Ni *K*-edge using Fluorescence mode. The in situ measurement was performed in 1 M KOH at various applied potentials within a potential range of oxygen evolution reaction (OER) at room temperature for un-confined Ni(OH)₂ and Ex-SnS₂ confined Ni(OH)₂. The spectra were collected after applying the potential for at least 25 min to ensure that the system has reached a steady-state.[26] Prior to XAS measurement, the Ex-SnS₂ confined Ni(OH)₂ /carbon paper (CP) electrodes were prepared by dropping the catalyst ink. The XAS results obtained in transmission mode were analyzed with DEMETER software package.[27]

Electrochemical Measurements: The electrochemical performances of the as-prepared samples were studied with a standard three-electrode system where Ag/AgCl/sat. KCl, graphite rod, and Ex-SnS₂ confined Ni(OH)₂ casted on carbon paper act as a reference, counter, and working electrode, respectively, in 1 M KOH electrolyte. The ink was prepared by dispersing 7 mg of the sample and 50 µL of Nafion solution (0.05 wt.% in alcohol) in 1 mL of isopropanol and distilled water (3:1) followed by ultrasonication for 1 h to form a homogeneous catalyst ink. Later, 70 µL of catalyst ink was drop cast on a carbon paper (1 × 2 cm^2). The LSV curves were measured at a scan rate of 1 mV s^{-1} and CV at a scan rate of 10 mV s^{-1} were collected. Before the electrochemical measurement, the electrolyte was saturated with argon (Ar > 99.99) for 20 min to remove dissolved oxygen in KOH solution. The durability test was carried out through chronopotentiometry run at a current density of 10, 30, 100 mA cm^{-2}. Moreover, the electrochemical double-layer capacitance, which is expected to be linearly proportional to the ECSA, was determined by measuring the capacitive current at non-Faradic region from scan rate dependent CV runs.

Supporting Information

Supporting Information is available from the Wiley Online Library or from the author.

Conflict of Interest

The authors declare no conflict of interest.

Data Availability Statement

The data that support the findings of this study are available from the corresponding author upon reasonable request.

[1] K. B. Ibrahim, W.-N. Su, M.-C. Tsai, S. A. Chala, A. W. Kahsay, M.-H. Yeh, H.-M. Chen, A. D. Duma, H. Dai, B.-J. Hwang, *Nano Energy* **2018**, *47*, 309.

[2] T. A. Berhe, W.-N. Su, J.-H. Cheng, M.-H. Lin, K. B. Ibrahim, A. W. Kahsay, C. Lin Li, A. M. Tripathi, M.-T. Tang, B.-J. Hwang, *ChemistrySelect* **2020**, *5*, 3266.

[3] K. B. Ibrahim, M.-C. Tsai, S. A. Chala, M. K. Berihun, A. W. Kahsay, T. A. Berhe, W.-N. Su, B.-J. Hwang, *J. Chin. Chem. Soc.* **2019**, *66*, 829.

[4] K. B. Ibrahim, T. A. Shifa, P. Moras, E. Moretti, A. Vomiero, *Small*, **19**, 2204765.

[5] T. A. Shifa, A. Gradone, K. Yusupov, K. B. Ibrahim, M. Jugovac, P. M. Sheverdyaeva, J. Rosen, V. Morandi, P. Moras, A. Vomiero, *Chem. Eng. J.* **2023**, *453*, 139781.

[6] C. Roy, B. Sebok, S. B. Scott, E. M. Fiordaliso, J. E. Sørensen, A. Bodin, D. B. Trimarco, C. D. Damsgaard, P. C. K. Vesborg, O. Hansen, I. E. L. Stephens, J. Kibsgaard, I. Chorkendorff, *Nat. Catal.* **2018**, *1*, 820.

[7] T. A. Shifa, A. Vomiero, *Adv. Energy Mater.* **2019**, *9*, 1902307.

[8] K. J. Koski, C. D. Wessells, B. W. Reed, J. J. Cha, D. Kong, Y. Cui, *J. Am. Chem. Soc.* **2012**, *134*, 13773.

[9] K. J. Koski, J. J. Cha, B. W. Reed, C. D. Wessells, D. Kong, Y. Cui, *J. Am. Chem. Soc.* **2012**, *134*, 7584.

[10] K. P. Chen, F. R. Chung, M. Wang, K. J. Koski, *J. Am. Chem. Soc.* **2015**, *137*, 5431.

[11] A. C. Thenuwara, E. B. Cerkez, S. L. Shumlas, N. H. Attanayake, I. G. McKendry, L. Frazer, E. Borguet, Q. Kang, R. C. Remsing, M. L. Klein, *Angew. Chem.* **2016**, *128*, 10537.

[12] T. Yu, T. Hou, P. Shi, Y. Yang, M. Chen, W. Zhou, Z. Jiang, X. Luo, H. Zhou, C. Yuan, *Inorg. Chem.* **2022**, *61*, 2360.

[13] Z. Chen, K. Leng, X. Zhao, S. Malkhandi, W. Tang, B. Tian, L. Dong, L. Zheng, M. Lin, B. S. Yeo, K. P. Loh, *Nat. Commun.* **2017**, *8*, 14548.

[14] W. Li, D. Xiong, X. Gao, L. Liu, *Chem. Commun.* **2019**, *55*, 8744.

[15] W. Li, D. Chen, F. Xia, J. Z. Y. Tan, J. Song, W.-G. Song, R. A. Caruso, *Chem. Commun.* **2016**, *52*, 4481.

[16] M. G. Sendeku, F. Wang, Z. Cheng, P. Yu, N. Gao, X. Zhan, Z. Wang, J. He, *ACS Appl. Mater. Interfaces* **2021**, *13*, 13392.

[17] S. Anantharaj, S. R. Ede, K. Sakthikumar, K. Karthick, S. Mishra, S. Kundu, *ACS Catal.* **2016**, *6*, 8069.

[18] L. Peng, S. S. A. Shah, Z. Wei, *Chin. J. Catal.* **2018**, *39*, 1575.

[19] B. R. Wygant, K. Kawashima, C. B. Mullins, *ACS Energy Lett.* **2018**, *3*, 2956.

[20] O. Mabayoje, A. Shoola, B. R. Wygant, C. B. Mullins, *ACS Energy Lett.* **2016**, *1*, 195.

[21] Q. Fu, X. Bao, *Chem. Soc. Rev.* **2017**, *46*, 1842.

[22] S. Parvin, V. Hazra, A. G. Francis, S. K. Pati, S. Bhattacharyya, *Inorg. Chem.* **2021**, *60*, 6911.

[23] Z. Y. Wang, W. Xia, G. Q. Huang, *Phys. C* **2017**, *543*, 52.

[24] J. He, Y. Zou, Y. Huang, C. Li, Y. Liu, L. Zhou, C.-L. Dong, X. Lu, S. Wang, *Sci. China: Chem.* **2020**, *63*, 1684.

[25] J. Yan, L. Kong, Y. Ji, J. White, Y. Li, J. Zhang, P. An, S. Liu, S.-T. Lee, T. Ma, *Nat. Commun.* **2019**, *10*, 2149.

[26] H.-L. Yu, K. B. Ibrahim, P.-W. Chi, Y.-H. Su, W.-T. Chen, S.-C. Tseng, M.-T. Tang, C.-L. Chen, H.-Y. Tang, C.-W. Pao, K.-H. Chen, M.-K. Wu, H.-L. Wu, *Adv. Funct. Mater.* **2022**, *32*, 2112394.

[27] B. Ravel, M. Newville, A. Athena, *J. Synchrotron Radiat.* **2005**, *12*, 537.

[28] Z. Cai, B. Liu, X. Zou, H.-M. Cheng, *Chem. Rev.* **2018**, *118*, 6091.

[29] S. J. R. Tan, I. Abdelwahab, Z. Ding, X. Zhao, T. Yang, G. Z. J. Loke, H. Lin, I. Verzhbitskiy, S. M. Poh, H. Xu, C. T. Nai, W. Zhou, G. Eda, B. Jia, K. P. Loh, *J. Am. Chem. Soc.* **2017**, *139*, 2504.

[30] J. Jian, X. Kou, H. Wang, L. Chang, L. Zhang, S. Gao, Y. Xu, H. Yuan, *ACS Appl. Mater. Interfaces* **2021**, *13*, 42861.

[31] C. Luan, G. Liu, Y. Liu, L. Yu, Y. Wang, Y. Xiao, H. Qiao, H. Dai, X. Zhang, *ACS Nano* **2018**, *12*, 3875.

[32] X.-J. Lv, G.-W. She, S.-X. Zhou, Y.-M. Li, *RSC Adv.* **2013**, *3*, 21231.

[33] B. Li, L. Jiang, X. Li, P. Ran, P. Zuo, A. Wang, L. Qu, Y. Zhao, Z. Cheng, Y. Lu, *Sci. Rep.* **2017**, *7*, 11182.

[34] K. B. Ibrahim, W. N. Su, M. C. Tsai, A. W. Kahsay, S. A. Chala, M. K. Birhanu, J. F. Lee, B. J. Hwang, *Mater. Today Chem.* **2022**, *24*, 100824.

[35] S. A. Chala, M.-C. Tsai, W.-N. Su, K. B. Ibrahim, B. Thirumalraj, T.-S. Chan, J.-F. Lee, H. Dai, B.-J. Hwang, *ACS Nano* **2020**, *14*, 1770.

[36] X. Zhang, M. Jin, F. Jia, J. Huang, A. Amini, S. Song, H. Yi, C. Cheng, *Energy Environ. Mater.* **2022**, *0*, e12457.

[37] S. A. Chala, M.-C. Tsai, W.-N. Su, K. B. Ibrahim, A. D. Duma, M.-H. Yeh, C.-Y. Wen, C.-H. Yu, T.-S. Chan, H. Dai, B.-J. Hwang, *ACS Catal.* **2019**, *9*, 117.

[38] O. Diaz-Morales, D. Ferrus-Suspedra, M. T. M. Koper, *Chem. Sci.* **2016**, *7*, 2639.

[39] F. Lei, W. Liu, Y. Sun, J. Xu, K. Liu, L. Liang, T. Yao, B. Pan, S. Wei, Y. Xie, *Nat. Commun.* **2016**, *7*, 12697.

[40] D. González-Flores, K. Klingan, P. Chernev, S. Loos, M. R. Mohammadi, C. Pasquini, P. Kubella, I. Zaharieva, R. D. L. Smith, H. Dau, *Sustainable Energy Fuels* **2018**, *2*, 1986.

[41] F. Song, M. M. Busch, B. Lassalle-Kaiser, C.-S. Hsu, E. Petkucheva, M. Bensimon, H. M. Chen, C. Corminboeuf, X. Hu, *ACS Cent. Sci.* **2019**, *5*, 558.

[42] D. Friebel, M. W. Louie, M. Bajdich, K. E. Sanwald, Y. Cai, A. M. Wise, M.-J. Cheng, D. Sokaras, T.-C. Weng, R. Alonso-Mori, R. C. Davis, J. R. Bargar, J. K. Nørskov, A. Nilsson, A. T. Bell, *J. Am. Chem. Soc.* **2015**, *137*, 1305.

[43] M. K. Birhanu, M.-C. Tsai, A. W. Kahsay, C.-T. Chen, T. S. Zeleke, K. B. Ibrahim, C.-J. Huang, W.-N. Su, B.-J. Hwang, *Adv. Mater. Interfaces* **2018**, *5*, 1800919.

[44] K. M. Ø. Jensen, M. Christensen, P. Juhas, C. Tyrsted, E. D. Bøjesen, N. Lock, S. J. L. Billinge, B. B. Iversen, *J. Am. Chem. Soc.* **2012**, *134*, 6785.